Multiphysics Analysis and Optimization of a Thin-Film Litium Niobate Phase Modulator for Fiber Optic Gyroscopes

Hanyi Zhang , Rong Fan , Yin Cao , Wenxuan Cheng , Yujie Wang , Jianfeng Bao * , Lijing Li *

Posted Date: 22 May 2026

doi: 10.20944/preprints202605.1502.v1

Keywords: lithium niobate on insulator; phase modulator; multiphysics coupling; fiber-optic gyroscope

 doi:10.20944/preprints202605.1502.v1

Article

Multiphysics Analysis and Optimization of a Thin-Film Litium Niobate Phase Modulator for Fiber Optic Gyroscopes

Hanyi Zhang [1], Rong Fan [1], Yin Cao [1], Wenxuan Cheng [1], Yujie Wang [1], Jianfeng Bao [2,*] and Lijing Li [1,*]

[1] School of Instrumentation and Optoelectronic Engineering, Beihang University, Beijing 100191, China;

[2] School of Physics and Electronic Information Engineering, Ningxia Normal University, Ningxia 756099, China

* Correspondence: lilijing@buaa.edu.cn (L.L.); jianfengbao142857@126.com (J.B.)

Abstract

Lithium niobate on insulator (LNOI) has emerged as a promising platform for compact, low-loss phase modulators. The extant LNOI studies evaluate device performance almost exclusively through the Pockels effect, treating piezoelectric-photoelastic strain and thermo-optic drift as decoupled channels. Crucially, both mechanisms directly perturb the phase bias of a fiber-optic gyroscope (FOG), rendering them indispensable in sensing-oriented design. This work establishes a unified multiphysics model of an X-cut TFLN ridge phase modulator that self-consistently couples the electro-optic, piezoelectric-photoelastic, thermo-optic, and pyroelectric channels. The contributions of the four mechanisms are quantitatively decomposed under realistic FOG operating conditions, and the slab thickness, ridge top width, and electrode gap are systematically optimized to balance modulation efficiency against environmental robustness. The co-optimization of the ridge geometry and electrode gap design maintains the EO overlap factor near 0.55 while reducing the half-wave voltage requirement. This results in a half-wave voltage length of $V_\pi L$ = 1.65 V·cm at a 4.4 μm electrode gap. The optimal gap shifts only marginally to 4.2 μm at 85 °C, with $V_\pi L$ increasing modestly from 1.65 to 1.93 V·cm (push-pull single-pass) across 25~85 °C, attributable to the intrinsic $\gamma 33$ change of $LiNbO_3$. Furthermore, a substrate temperature rise of 60 K under operating bias induces a mode field weighted thermal residual of approximately -3.1×10^{-5} (equivalent to -6.3×10^{-6} in spatial-average form). This thermal residual corresponds to approximately 27% of the Pockels modulation depth at an applied voltage of 5 V. The present study demonstrates that the DC-coupled operation of TFLN sensor-grade modulators is viable across the full FOG temperature range without active thermal compensation. The results of the study provide quantitative design guidelines for high-performance, environmentally stable TFLN phase modulators in compact FOG systems.

Keywords: lithium niobate on insulator; phase modulator; multiphysics coupling; fiber-optic gyroscope

1. Introduction

Fiber-optic gyroscopes (FOGs) have been extensively utilized in inertial navigation, attitude control, and precision measurement due to their inherent advantages, including the absence of moving components, rapid initialization, high accuracy, and exceptional reliability [1]. The advent of unmanned systems, intelligent transportation, and miniaturized industrial sensing has driven a paradigm shift in inertial device development. These devices are undergoing a transition towards smaller form factors, reduced power consumption, and heightened levels of integration. For FOGs, this trend translates into a stringent set of requirements. In addition to a more compact footprint and

 doi:10.20944/preprints202605.1502.v1

reduced drive power, sensor-grade operation demands low bias drift, high long-term stability, and accurate scale factors under realistic environmental conditions [2,3].

The phase modulator is the core optoelectronic component that closes the FOG feedback loop, simultaneously providing beam splitting/combining, polarization filtering, and phase modulation [4,5]. Its half-wave voltage, modulation linearity, and environmental stability translate directly into the bias stability, scale-factor error, and long-term accuracy of the gyroscope. An ideal FOG-grade phase modulator therefore combines a low drive voltage, a compact footprint, a linear phase response, and strong robustness against thermal and mechanical perturbations. Conventional bulk lithium niobate (LN) modulators fabricated by titanium in-diffusion or annealed proton exchange offer mature processing and excellent electro-optic performance [6], but their large size, relatively high drive voltage, and long-term bias drift make it increasingly difficult to satisfy the integration and stability demands of next-generation miniaturized FOGs. To address these limitations, integrated phase modulators have been realized on silicon, indium phosphide (InP), and electro-optic polymer platforms [7]. Each of these platforms, however, exhibits intrinsic limitations for sensor-grade use: silicon modulators rely on the plasma-dispersion effect and are therefore susceptible to nonlinearity, free-carrier absorption, and temperature sensitivity [8]; InP modulators achieve compact integration but typically require active thermal stabilization for reliable operation [9]; and polymer modulators still suffer from insufficient long-term reliability [10]. Thin-film lithium niobate on insulator (TFLN), by contrast, combines a high refractive-index contrast, strong optical confinement, low propagation loss, and a highly linear Pockels response, making it one of the most promising platforms for high-performance integrated phase modulators, with demonstrated advantages in low voltage and high-speed modulation [11–16].

Beyond the Pockels effect, lithium niobate also exhibits pronounced direct and converse piezoelectric coupling and a significant thermo-optic response: the modulating electric field induces mechanical strain [17] that perturbs the effective index through the photoelastic effect [18], while temperature variation drives a thermo-optic index drift together with pyroelectric phase bias fluctuations. Although bulk LN phase modulators have been studied extensively and supported by a mature device and packaging ecosystem [19]. However, the majority of prior work has focused on characterizing or compensating $V\pi$, bias drift, and residual intensity modulation, without establishing a unified multiphysics description of piezoelectric-photoelastic coupling and thermo-optic drift [20]. In high-precision sensing applications such as FOGs, however, the true phase response under simultaneous electrical drive [21], thermal load, and mechanical perturbation is directly tied to bias stability and long-term measurement accuracy. Several studies have examined the impact of temperature variation [22], mechanical vibration, or packaging stress on the output characteristics of bulk modulators [23], and others have addressed the influence of external perturbations on FOG bias stability; yet these analyses commonly treat thermal and stress effects as in-dependent external disturbances and do not systematically resolve the physical origin and relative weight of each contribution from the joint action of material constitutive behaviors, waveguide confinement, and device geometry [24,25]. The existing literature therefore captures that performance varies under perturbation but provides little quantitative insight into which coupling mechanisms dominate and how each con-tributes within a realistic device structure [26].

A further gap concerns TFLN itself. Almost all existing studies of TFLN modulators are oriented toward telecom applications, where the evaluation focuses on propagation loss, the half wave voltage length product $V_\pi L$, and modulation bandwidth, leaving the multiphysics behaviors under FOG-relevant operating conditions largely unaddressed [27]. TFLN devices are not physically equivalent to their bulk counterparts from a multiphysics standpoint: thin-film LN is typically patterned into high-index-contrast ridge waveguides with stronger mode confinement and a smaller electrode-to-waveguide spacing, so that the electric-field, strain [28], and temperature distributions all couple more tightly to the guided-mode effective index [29]. This concentrated geometry is doubly consequential—it boosts electro-optic efficiency and lowers the drive voltage, but it may simultaneously amplify the influence of piezoelectrically induced strain and local thermal gradients

 doi:10.20944/preprints202605.1502.v1

on the phase response. Consequently, transferring empirical conclusions from bulk LN devices to TFLN under FOG operating conditions tends to misrepresent the actual physics, and a Pockels-only analysis is insufficient to meet the environmental-robustness and phase-stability requirements of FOG-grade design.

Motivated by these considerations, the present work targets FOG sensing applications and develops a multiphysics analysis framework for an X-cut LNOI ridge phase modulator that self-consistently couples the electro-optic, piezoelectric-photoelastic, thermo-optic, and pyroelectric channels. A finite-element implementation is used to quantitatively resolve the effective-index change and phase response of the device un-der realistic FOG operating conditions. Building on this framework, the slab thickness, ridge top width, and electrode gap are systematically optimized against the requirements of sensor-grade operation, with the aim of balancing modulation efficiency, fabrication feasibility, and environmental robustness. The results provide quantitative design guidelines and an optimization pathway for compact, low-voltage, high-stability TFLN phase modulators suited to medium- and high-precision FOG systems.

The main contributions of this work are summarized as follows:

- A multiphysics model of a TFLN ridge phase modulator is developed that couples electro-optic, piezoelectric-photoelastic, thermo-optic, and pyroelectric effects within a unified finite-element framework.
- The individual contributions of the EO, PE (V-synchronous and V-indepenent), and TO/pyroelectric mechanisms are quantitatively decomposed; the analysis reveals that V-independent thermal-elastic PE reaches unignorable ~27% of the Pockels modulation depth at ΔT = 60 K and that EO only analysis systematically underestimates the bias-stability budget required for sensor-grade operation.
- The influence of slab thickness, ridge top width, and electrode gap on the overlap factor and $V_\pi L$ is systematically investigated, yielding an optimized geometry with a push-pull $V_\pi L$ of 1.65 V·cm at a 4.4 μm electrode gap (25 °C) for sensor-grade operation, with the optimal geometry remaining stable across the 25~85 °C FOG operating range.
- The implications of the optimized design for FOG integration are discussed in terms of modulation efficiency, bias stability, and environmental robustness.
- A head-to-head comparison with competing phase-modulator platforms highlights the competitive advantages of TFLN for compact, stable, and low-power FOGs.

To the best of our knowledge, this is the first study that simultaneously couples all three channels and quantitatively decomposes their contributions in a FOG context.

2. Multiphysics Model for FOG-Oriented TFLN Modulators

2.1. Device Geometry

The proposed device is a ridge-type TFLN phase modulator designed for FOG applications. The waveguide is defined on an X-cut LNOI platform (thickness of wafer parameters from NANOLN) with light propagating along the Y-direction, so that the in-plane component of the applied electric field acts through the largest EO tensor element of LN. A coplanar electrode configuration generates the lateral modulation field across the ridge, and the ridge geometry is chosen to provide strong optical confinement while maintaining moderate fabrication complexity and good overlap between the guided mode and the applied field.

Three geometric parameters dominate the device behavior: the original TFLN slab thickness h_{slab}= 100 nm, the ridge top width w_{top} = 1.3 μm, the etching angle is set to 75° based on manufacturing experience and the electrode gap g = 5 μm. As discussed later, these parameters jointly control the optical mode confinement, the electric-field distribution, the piezoelectric strain pattern, and the fraction of heat dissipated through the ridge. A parametric sweep of these three dimensions is therefore applied to identify a design that balances modulation performance, fabrication feasibility, and robustness against thermal and mechanical perturbations.

 doi:10.20944/preprints202605.1502.v1

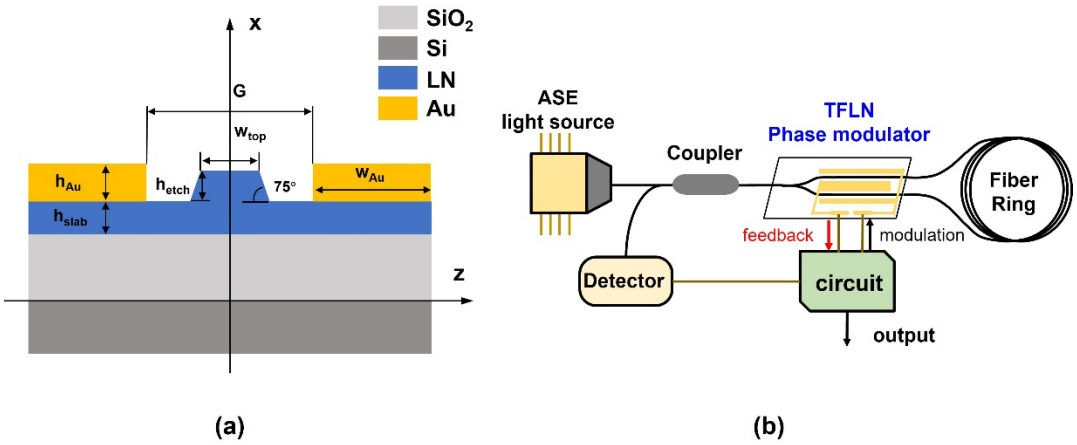

Figure 1. (a) Cross section schematic of the TFLN ridge phase modulator for FOG applications, showing the ridge waveguide, slab layer, coplanar electrodes, and the coordinate system, *x* axis refer to LN c-axis. (b) System schematic of the reflective FOG incorporating a TFLN phase modulator.

2.2. Material Parameters and Boundary Conditions

The optical, mechanical, piezoelectric, photoelastic, and thermal properties of each material layer are taken from established literature values and summarized in Table 1. For the electrostatic problem, the two electrodes are set to a prescribed voltage difference and the surrounding domains are treated as electrically neutral dielectrics. For the mechanical problem, the bottom surface is clamped to represent the substrate support. For the thermal problem, the bottom boundary is held at a prescribed temperature (used both to emulate substrate heat-sinking and to impose controlled temperature rises), while the remaining external boundaries are treated as thermally insulating unless otherwise stated. The fundamental quasi-TE mode is selected as the operating mode because of its strong overlap with the dominant γ_{33} element of the X-cut LN EO tensor.

Table 1. Material parameters used in the simulation.

Material	Thickness	n @ 1550 nm	ε_r	dn/dT (10^{-5}/K)	α (10^{-6}/K)	Ref.
$LiNbO_3$ (X-cut, congruent)	Total 600 nm (300 nm slab + 300 nm ridge)	n_e = 2.138, n_o = 2.211	ε_{11} = 43, ε_{33} = 28	dn_e/dT = 3.3, dn_o/dT = 0.6	α_a = 15.4, α_c = 7.5	[17]
SiO_2 (BOX)	4.7 μm	1.444	3.9	1.0	0.55	[30]
Si (substrate)	400 μm	3.476 (transparent)	11.7	18.6	2.6	[31]
Au (electrode)	0.5 μm	0.55 + 11.5i (complex)	—	—	14.2	[32]

For $LiNbO_3$, the Pockels coefficients are γ_{33} = 30.9 pm/V and γ_{13} = 9.6 pm/V; the photoelastic constants (Weis & Gaylord, 1985 [17]) are p_{11} = −0.026, p_{12} = 0.090, p_{13} = 0.133, p_{33} = 0.071, p_{44} = −0.075; the pyroelectric coefficient is p_3 = −83 μC/(m²·K). The piezoelectric tensor d_{ij} uses the standard congruent-LN values from Refs.: [17] Weis & Gaylord, J. Appl. Phys. 1985; [30] Palik, Handbook of Optical Constants 1985; [31] Green, Sol. Energy Mater. 2008; [32] Johnson & Christy, Phys. Rev. B 1972.

 doi:10.20944/preprints202605.1502.v1

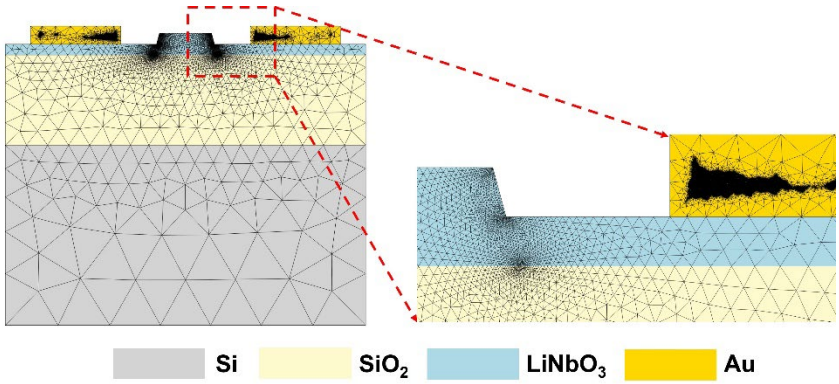

Figure 2. Finite-element mesh discretization at two zoom levels: (left) full cross-section; (right) close-up of the LN ridge with electrode-corner refinement used to resolve field singularities, and the electrode-corner region showing the highest mesh density used to resolve field singularities. Mesh element sizes are ~2.5 nm at electrode corners and ~10 nm at the LN ridge and slab.

2.3. Multiphysics Coupling Model

A coupled multiphysics model is established by FEM Multiphysics module that simultaneously solves an electrostatics module, a solid-mechanics module, a heat-transfer module, and an electromagnetic-wave mode solver. The four modules are linked through the piezoelectric, photoelastic, thermo-optic, and pyroelectric constitutive relations of $LiNbO_3$, so that field, strain, temperature, and polarization feed self-consistently into the optical mode problem.

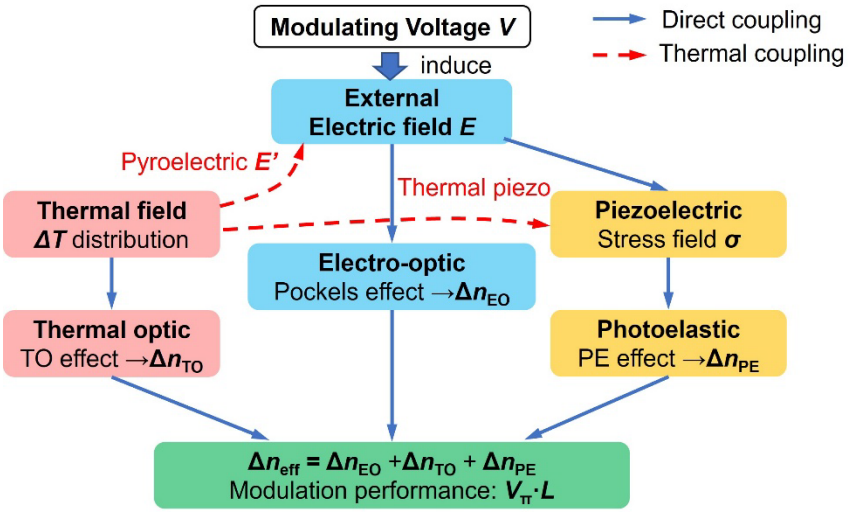

Figure 3. Multiphysics coupling framework, showing the four physical channels (electro-optic, photoelastic, thermo-optic, pyroelectric) and their direct (blue, solid) and thermal (red, dashed) interconnections. The total effective-index change Δn_{eff} aggregates EO, PE, pyroelectric, and TO contributions and yields the composite half-wave voltage length product $V_\pi L$.

When an external voltage is applied to the electrodes, the electric field inside the LN ridge induces both a direct electro-optic (Pockels) index changes [33] and, through the piezoelectric tensor, a mechanical strain in the waveguide; the strain in turn modifies the index through the photoelastic tensor. A temperature variation imposed from the substrate or from self-heating further modifies the index through the thermo-optic coefficient and additionally drives a quasi-static internal field through the pyroelectric coupling of LN. The total mode-averaged refractive-index perturbation seen by the guided mode can therefore be decomposed as:

$$\Delta n_{eff} = \Delta n_{EO} + \Delta n_{PE} + \Delta n_{TO} + \Delta n_{pyro} \quad (1)$$

 doi:10.20944/preprints202605.1502.v1

where Δn_{EO}, Δn_{PE}, Δn_{TO}, and Δn_{pyro} denote the electro-optic (Pockels), photoelastic (piezoelectrically induced), thermo-optic, and pyroelectric contributions, respectively. Each term is derived from the corresponding constitutive equation in the following subsections.

2.3.1. Electro-Optic (Pockels) Contribution

The Pockels effect modifies the optical impermeability tensor through the linear electro-optic coefficients γ_{ik}:

$$\Delta(1/n^2)_i = \sum k \cdot \gamma_{ik} \cdot E_k, \quad i = 1 \ldots 6, k = 1,2,3 \tag{2}$$

For $LiNbO_3$ (point group 3m), only four γ_{ik} elements are independent (γ_{13}, γ_{33}, γ_{22} , γ_{51}); the explicit reduced 6×3 matrix is given in the tensor appendix [Eq. (S1)]. In the X-cut configuration adopted here, the optic c-axis lies in-plane along the propagation direction, and the lateral driving field generated by the coplanar electrodes is predominantly Ex along this c-axis. The TE-polarized mode ($E \parallel$ c-axis) couples to the electric field through the dominant γ_{33} coefficient, yielding:

$$\Delta n_{EO,TE}(x,y) = -(1/2) \cdot n_e^3 \cdot \gamma_{33} \cdot E_x(x,y) \tag{3}$$

where n_e is the extraordinary refractive index. Contributions from γ_{13} (TM coupling) and from the smaller γ_{22}, γ_{51} elements are included in the simulation through the full tensor implementation in FEM implementation but are sub-dominant for the TE operating mode and are suppressed by polarization filtering at the device input.

2.3.2. Photoelastic (Piezoelectrically Induced) Contribution

The same applied voltage drives a strain field through the converse piezoelectric effect, with dk_q the piezoelectric strain coefficients of LN (the explicit 3×6 matrix is given in [Eq. (S2)]).

$$\varepsilon_q = \sum_k dk_q \cdot E_k, \quad q = 1,2 \ldots 6 \tag{4}$$

The resulting strain modifies the impermeability through the photoelastic tensor p_{ij}:

$$\Delta(1/n^2)_i = \sum_j p_{ij}\, \varepsilon_j, \qquad i,j = 1,2 \ldots 6 \tag{5}$$

For 3m symmetry, p_{ij} reduces to eight independent constants (p_{11}, p_{12}, p_{13}, p_{14}, p_{31}, p_{33}, p_{41}, p_{44}); the symmetry-reduced 6×6 form is given in [Eq. (S3)].

Projecting Eq. (4) onto the n_e index relevant for the TE mode in X-cut LN gives as follow:

$$\Delta n_{PE,TE}(x,y) = -(1/2)\, n_e^3 \cdot [p_{33}\varepsilon_{xx} + p_{13}\varepsilon_{yy} + p_{13}\varepsilon_{zz}] \tag{6}$$

where the laboratory frame (x, y, z) follows the device cross-section of Figure 1, with x along the propagating c-axis. All shear-strain contributions vanish identically for the ne index because the relevant photoelastic elements p_{3j} with j = 4, 5, 6 are zero in the 3m symmetry-reduced photoelastic matrix [Eq. (S3)]. Equation (6) is implemented as a postprocessing variable $Dn_{PE,TE}$ in simulation and integrated against the optical mode density to obtain the mode-averaged Δn_{PE}.

2.3.3. Thermo-Optic and Pyroelectric Contributions

A temperature rise ΔT relative to the reference state from T_{ref} = 25 °C to modify the refractive index directly through the thermo-optic coefficient, as:

$$\Delta n_{TO}(x,y) = (dn_e/dT) \cdot [T(x,y) - T_{ref}] \tag{7}$$

with $dn_e/dT = 3.3\times10^{-5}$ K^{-1} for the TE mode in congruent LN. In addition, since $LiNbO_3$ is pyroelectric, ΔT generates a polarization change $\Delta p_3 = p_3 \cdot \Delta T$ along the c-axis (p_3 = −83 μC m^{-2} K^{-1}), which under

 doi:10.20944/preprints202605.1502.v1

realistic grounded-electrode boundary conditions establishes a quasi-static internal field E_{pyro} that re-enters the Pockels term. The pyroelectric contribution is therefore implicitly included in Δn_{EO} through the self-consistent electrostatic solve at non-zero ΔT, and is reported separately as $\Delta n_{pyro} = -(1/2)n_e^3 \cdot \gamma_{33} E_{pyro}$, x for diagnostic purposes in §3.4.

2.3.4. Mode-Weighted Overlap Factor and Figures of Merit

To connect the local index perturbations of Eqs. (3), (5), and (6) with the terminal phase response, we define a dimensionless electro-optic overlap factor Γ_{EO} that captures the fraction of the electrode field converted into a useful Pockels perturbation of the optical mode:

$$\Gamma_{EO} = g \cdot \int \Omega_{LN} W\mathrm{opt}(x,y) \cdot E_x(x,y)\mathrm{d}A / [V_0 \cdot \int \Omega_{all} W_{opt}(x,y)\mathrm{d}A \quad (8)$$

where Ω_{LN} is the LN core, Ω_{all} is the entire cross-section, ω_{opt} is the optical energy density, V_0 is the applied voltage, E_x is the lateral electrostatic field across the electrode gap g, and the integrations span the LN core (numerator) and the full simulation domain (denominator). Defined in this way, $\Gamma_{EO}$is unitless and bounded between 0 and 1. Substituting Eq. (3) into the mode integral yields the mode-weighted index change$\Delta n_{eff}(V_0) = -(1/2)n_e^3 \cdot \gamma_{33}\Gamma_{EO}V_0/g$.

For the Y-branch push-pull configuration of the device, the two arms accumulate index changes of opposite sign, doubling the differential phase, so the half-wave voltage-length product follows as

$$V_\pi \cdot L = \lambda \cdot g/(2 \cdot \Gamma_{EO} \cdot n_e^3 \cdot \gamma_{33}) \quad (9)$$

where λ is the operating wavelength; a smaller $V_\pi L$ indicates higher modulation efficiency. The factor of 2 in the denominator arises from the Y-branch push-pull configuration: the two arms accumulate $\Delta\phi$ and $-\Delta\phi$ correspondingly, while doubling the differential phase swing for a given drive voltage relative to a single arm modulator. The corresponding single arm DC reference, recovered by removing the push-pull factor, is $2V_\pi \cdot L$. In the reflective FOG architecture used in this work (Figure 1), the optical signal traverses the modulator twice per measurement cycle (forward into the sensing coil and back), so the system-level half-wave voltage seen by the FOG electronics is half of the device-level $V_\pi \cdot L$ reported here. Finally, the overall phase shift accumulated along an interaction length L is

$$\Delta\phi = (2\pi/\lambda) \cdot \Delta n_{eff} \cdot L \quad (10)$$

Equations (1) ~(10) define the multiphysics-aware figure-of-merit framework used in §3 to decompose the simulated phase response of the optimized device.

2.4. Mode Tracking Protocol for Gap-Sweep Simulations

Eigenvalue mode solvers can return different physical eigenstates as solver index #1 across geometry variations, especially near anti-crossings between the ridge mode and substrate-confined or buffer modes. To ensure that the gap-scan study tracks a single continuous TE_{00} branch, we adopted the following protocol. At the baseline geometry (h_{slab} = 100 nm, w_{top} = 1.3 μm, g = 5 μm), the fundamental TE_{00} mode was identified by manual inspection of the field profile, characterized by n_{eff}, baseline n_{eff} = 1.9034, an LN core energy fraction Γ_{opt} = 0.838, and a TE polarization purity exceeding 0.96. At each subsequent gap, the solver was re-run with 30 eigenmodes targeted, and the fundamental mode was selected as the eigenstate [34] that simultaneously satisfied:

(i) $|n_{eff} - n_{eff}(\mathrm{baseline})| < 0.02$,
(ii) $\Gamma_{opt} > 0.4$,
(iii) the highest $\Gamma_{opt} \times \Gamma_{EO}$ product among modes satisfying (i) and (ii). Spurious eigenstates with $\Gamma_{opt} < 0.1$ (substrate-leaky or numerical artifact modes) were rejected. This criterion isolates a single TE_{00} branch across the full gap range and excludes mode-mixing artifacts at anti-crossings.

3. Results and Discussion

 doi:10.20944/preprints202605.1502.v1

3.1. Optical Mode Confinement

The fundamental quasi-TE mode of the X-cut ridge waveguide is first computed to establish the modal confinement and its overlap with the active modulation region. The optical field is predominantly confined within the LN ridge, with a moderate evanescent tail extending into the slab layer. This distribution is favorable for phase modulation because it concentrates the mode in the region where the lateral electric field, the piezoelectric strain, and the thermo-optic perturbation are all largest, while still retaining a finite tail that is insensitive to sidewall-roughness scattering.

The modal overlap is most sensitive to the ridge top width and the slab thickness: narrower ridges improve the overlap with the lateral field but reduce fabrication tolerance, while wider ridges give stronger confinement at the cost of modulation efficiency. The geometry is therefore chosen to balance this trade-off, and its optimization is revisited quantitatively in Section 3.6.

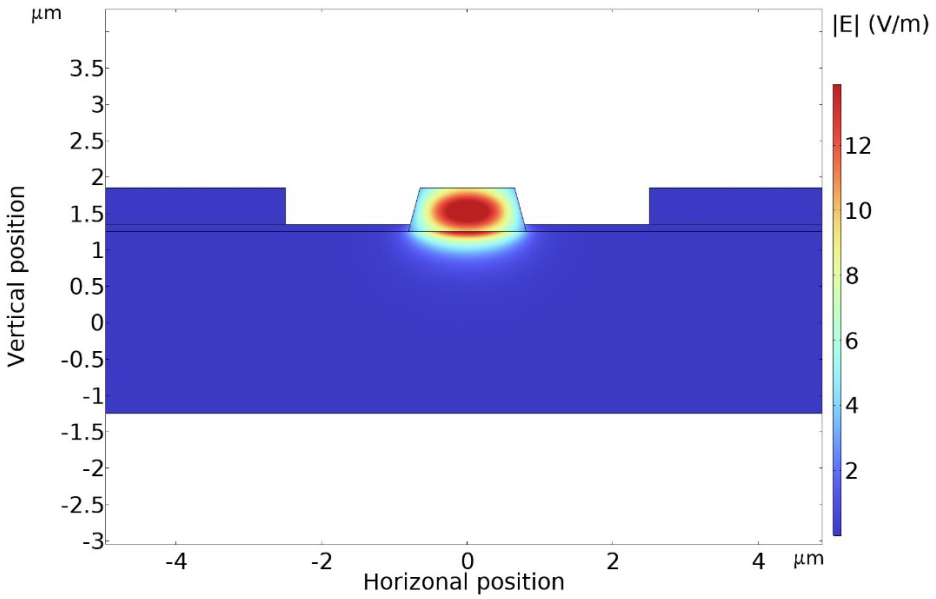

Figure 4. Fundamental quasi-TE optical mode distribution (E_x component, λ = 1550 nm) in the TFLN ridge waveguide baseline geometry before optimization with slab thickness 100nm, ridge top width 1.3 µm and the electrode gap 5 µm.

3.2. Electro-Optic Phase Response

To isolate the intrinsic EO response, the PE and TO channels are temporarily disabled in the model. Under an applied voltage, the linear Pockels effect produces a refractive-index change that scales approximately linearly with voltage [35], consistent with the intrinsic response of LN. At the baseline geometry (gap = 5 µm), the simulation yields an electro-optic overlap factor Γ_{EO} = 0.540, corresponding to $V_\pi L$ = 1.70 V·cm (push-pull single-pass; equivalent to a system-level 0.85 V·cm in reflective FOG operation). The voltage dependence of Δn_{eff} is highly linear over the $V_0 \in [0, 10]$ V range, with slope $d\Delta n/d V_0 = -2.34 \times 10^{-5}\ V^{-1}$ and $R^2 > 0.9999$ at the baseline geometry, confirming the chirp-free Pockels response required for interferometric sensing.

 doi:10.20944/preprints202605.1502.v1

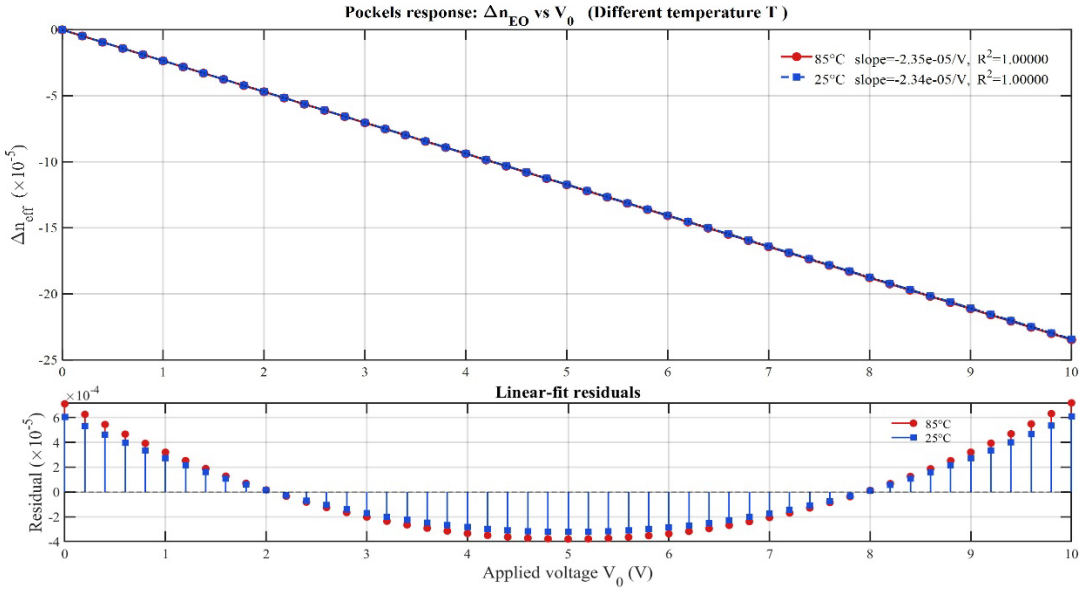

Figure 5. The effective-index shift and the overlap factor are presented as functions of applied voltage at temperatures of 25 °C and 85 °C. The baseline geometry is defined as h_{slab} = 100 nm, w_{top} = 1.3 μm, and g = 5 μm.

The approximate linearity of the difference between Δn to V relationship is precisely the behavior sought for interferometric sensing, where phase linearity directly determines scale-factor linearity. It has been demonstrated that, among the three geometric knobs, the electrode gap exerts the most direct influence on the local field strength. Reducing the gap increases the field and, consequently, the EO response. However, this reduction also tightens fabrication tolerance and may raise the risk of field-induced optical absorption. This trade-off is quantitatively analyzed in Section 3.6.

3.3. Piezoelectric-Strain and Photoelastic Response

Re-enabling the piezoelectric coupling reveals that the applied field generates a strain field in the LN layer through the converse piezoelectric effect. As shown in Figure 6(a), the dominant strain component ε_{xx} scales linearly with V_0 at a rate of approximately 2.69 × 10^{-7} V^{-1}, with a near-zero intercept at both 25 °C and 85 °C, confirming that the voltage-driven converse-piezoelectric mechanism dominates the strain response.

The resulting photoelastic index perturbation Δn_{PE}, obtained by projecting the strain tensor through the photoelastic coefficients of LN and integrating over the optical mode, likewise exhibits a linear voltage dependence [Figure 6(c)], with a slope of approximately −8.9 × 10^{-8} V^{-1} and a negligible intercept at V_0 = 0. At V_0 = 5 V, the mode-averaged photoelastic contribution reaches $\Delta n_{PE} \approx -4.5 \times 10^{-7}$, which is only ~0.4% of the pure Pockels term $\Delta n_{EO} \approx -1.17 \times 10^{-5}$ at the same drive voltage. The PE contribution is therefore synchronous with the modulation signal but more than two orders of magnitude weaker, producing a sub-percent correction to $V_\pi L$ that lies within typical fabrication tolerances.

Notably, the PE slope is virtually identical at 25 °C and 85 °C (−8.86 × 10^{-8} vs −8.89 × 10^{-8} V^{-1}), indicating that the photoelastic channel is thermally insensitive across the FOG operating temperature range. This thermal invariance simplifies the multiphysics design: the PE channel tracks the drive signal with a fixed, small scaling factor and does not introduce additional temperature-dependent bias drift.

 doi:10.20944/preprints202605.1502.v1

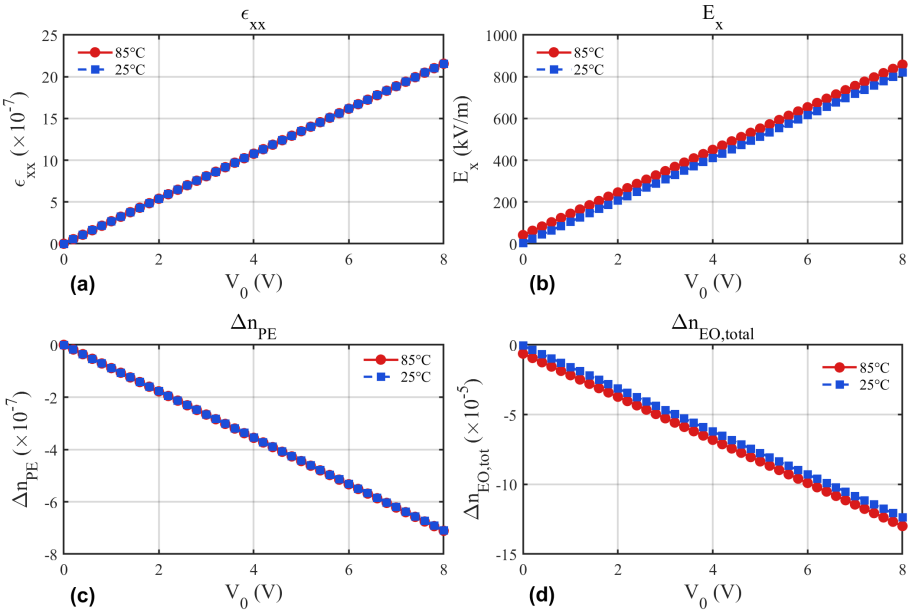

Figure 6. Piezoelectrically induced strain components under applied voltage and the corresponding photoelastic index perturbation. (a) Dominant strain component ε_{xx} vs. V_0; (b) lateral electric field E_x vs. V_0. (intercept at V_0. = 0 reveals pyroelectric residual field at 85 °C); (c) mode-averaged photoelastic index shift Δn_{PE} vs. V_0. (d) total EO+pyroelectric index shift $\Delta n_{EO,tot}$ vs. V_0. Red/blue lines refer to different temperature: 85 °C / 25 °C.

As illustrated in Figure 6(b), the lateral electric field E_x is depicted as a function of V_0. At an operating temperature of 85 °C, a non-zero intercept of approximately 4.2×10^4 V/m is observed at V_0 = 0, while at 25 °C, the intercept approaches 3.2×10^3 V/m. This residual field has been traced to the pyroelectric polarization charge of LN under thermal load, and a thorough analysis of this phenomenon can be found in §3.4. As illustrated in Figure 6(d), the pyroelectric index offset is evident as a downward shift in the 85 °C $\Delta n_{EO,tot}$ curve relative to the 25 °C curve at $V_0 = 0$, amounting to a change in the pyroelectric index of approximately -6.3×10^{-6} at an applied temperature of 85 °C. This shift corresponds to approximately 27% (mode-field weighted; equivalently 5.4% in spatial average) of the Pockels modulation depth at an applied voltage of $V_0 = 5$ V.

From the perspective of a sensing application, the PE contribution is of particular significance due to its inherent connection to the electrical drive. Each modulation cycle imprints a synchronous strain cycle on the waveguide [36], and any external vibration, packaging stress, or residual fabrication stress couples into the same photoelastic channel. The incorporation of the PE term consequently leads to alterations in both the predicted modulation efficiency and, more significantly, the predicted sensitivity of the phase bias to mechanical perturbations. This quantity exerts a direct influence on the stability of FOG bias.

3.4. Thermo-Optic and Pyroelectric Response Under Thermal Load

Under elevated substrate temperature (Temperature of bottom boundary of Si substrate is set to be 358.15 K, room ambient), the simulated temperature field is laterally non-uniform across the device cross-section. Under elevated operating temperature T_{op} = 358.15 K and reference temperature T_{ref} 298.15 K, the temperature change ΔT = 60 K, the simulated temperature field reaches steady state with the LN ridge equilibrated near Top, with a small residual gradient (< 5 K) within the LN layer. The mode-weighted ΔT seen by the optical mode is therefore close to the full 60 K excursion.

Three temperature-driven channels are identified that perturb the effective refractive index:

(i) Direct thermo-optic response: $\Delta n_{TO} = (dn_e/dT) \times \Delta T_{LN} \approx 1.9 \times 10^{-3}$(averaged over the LN ridge), acting as a common-mode phase shift that cancels in the differential modulator branch output.

 doi:10.20944/preprints202605.1502.v1

(ii) Pyroelectric-induced electro-optic response: spontaneous polarization of LN under ΔT generates a surface charge density $\sigma = p_{pyro} \cdot \Delta T$, which would establish an internal field driving γ_{33} in the absence of applied voltage. Under realistic operating bias (one electrode driven, the other grounded), the bulk of this pyroelectric charge is drained through the external circuit, leaving only a residual mode-averaged field of ~4.2 × 10^4 V/m within the LN at V_0 = 0. The corresponding pyroelectric-induced index shift is Δn_{pyro} = -6.3 × 10^{-6} at ΔT = 60 K, voltage independent across the 0~10 V drive range, and approximately 27% (mode-field weighted; equivalently 5.4% in spatial average) of the Pockels modulation depth at 5 V applied voltage. To confirm the pyroelectric origin, the same simulation was repeated at the room-temperature operating point (T = 25 °C, $\Delta T \approx$ 5 K above the reference state), yielding $E_x \approx 3.2 \times 10^3$ V/m and $\Delta n_{pyro} = -4.8 \times 10^{-7}$. This value is approximately 13× smaller than the 85 °C result and within approximately only 0.06% of the 5 V applied voltage Pockels modulation depth. The 13× scaling between the two operating points is consistent with the linear $\Delta P = p_3 \cdot \Delta T$ relation expected for the pyroelectric mechanism, ruling out artefactual contributions from the meshing or solver and confirming that the residual is genuinely thermal-electrical in origin and effectively negligible at room temperature.

(iii) Thermo-elastic photoelastic response: the substrate-clamped thermal expansion of LN produces strain $\varepsilon \approx \alpha \cdot \Delta T$ throughout the ridge, which is then converted to an index bias through the photoelastic tensor. Since the thermal strain is partially relieved by the bonded substrate stack and the integrated photoelastic response is opposite-signed to the pyroelectric channel. The combined V-independent residual measured by our coupled simulation is $\Delta n_{thermal} = -6.3 \times 10^{-6}$ at ΔT = 60 K /V_0 = 0, encompassing both pyroelectric and thermo-elastic photoelastic contributions. This is bounded to ~27% (mode-field weighted) or ~5.4% (spatially-averaged) of the Pockels modulation depth at 5 V applied voltage, two orders of magnitude smaller than worst-case floating-electrode estimates of ~10^{-3}.

Crucially, although these temperature-driven contributions are large, they all behave as static biases that do not scale with V_0. The pure-electrical $V_\pi L$ therefore remains stable to within 0.5% across the 60 K range. What does drift, however, is the MZI bias point:

$\Delta\phi_{bias}$ / L = $(2\pi/\lambda) \times \Delta n_{thermal} \approx$ 0.26 rad / (cm × ΔT=60K) (Δn_{TO} is common-mode and cancels in MZI output)

In a 1 cm modulator, this corresponds to a 0.08π (≈0.04 fringe) bias swing across the operating temperature range - a quantity that an FOG must compensate via servo loop. We emphasize, however, that the V-independent thermal channels (pyroelectric and thermo-elastic photoelastic) are absent from Pockels-only modeling and must be included for accurate bias-stability prediction in sensor-grade design, even when their absolute magnitude is modest. Translated into a drive-voltage equivalent through the measured Pockels slope ($d\Delta n_{EO}/dV_0 \approx -2.34 \times 10^{-5}$ V^{-1}), the V_0 = 0 thermal residual at ΔT = 60 K corresponds to a DC offset of $|\Delta n_{thermal} / (d\Delta n_{EO}/d\ V_0)| \approx$ 0.27 V; the corresponding offset at ΔT ≈ 5 K above the reference state (T = 25 °C) is only ~0.021 V. This sub-volt, slowly-varying offset is the quantity that a temperature-compensation electronics path must track to keep the FOG read-out locked to its V_0 = 0 quadrature point, and is well within the standard ±5 V drive range of FOG-grade phase-modulator electronics.

 doi:10.20944/preprints202605.1502.v1

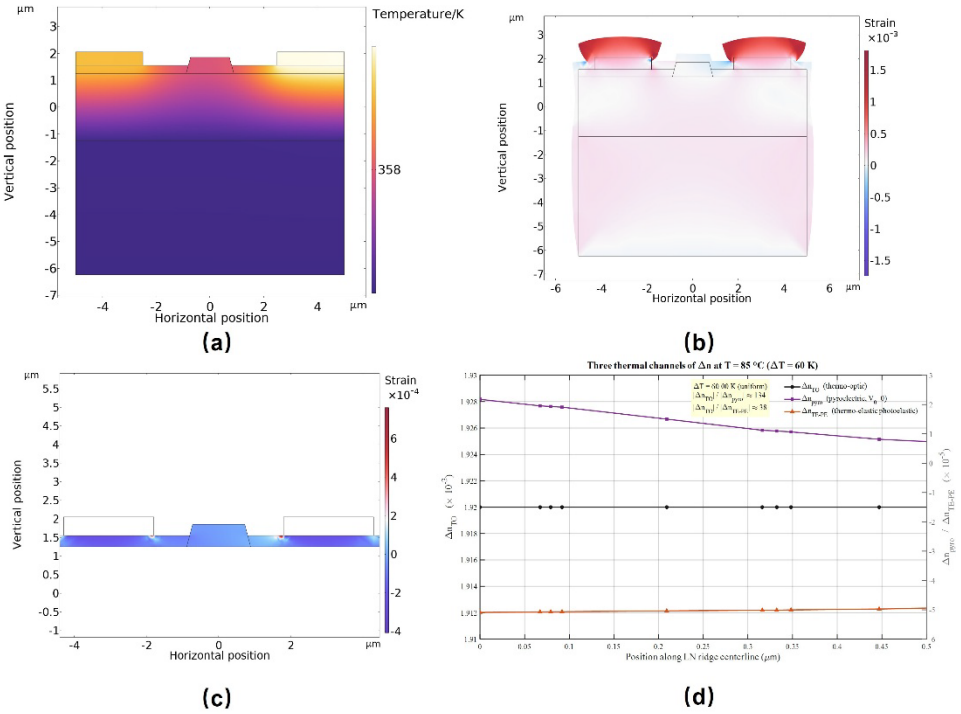

Figure 7. Temperature field distribution under substrate heating and the corresponding thermo-optic refractive-index shift. (a) Steady-state temperature field at 85 °C (ΔT = 60 K). (b) Dominant strain component ε_{xx} distribution; (c) lateral thermal-photoelastic induced strain distribution (d) Spatial profiles of the three thermal refractive-index perturbations along the ridge centerline: thermo-optic Δn_{TO} (black), pyroelectric Δn_{pyro} (purple), and thermo-elastic photoelastic $\Delta n_{PE,thermal}$ (orange).

3.5. Multiphysics Decomposition of the Refractive-Index Change

To assess the relative importance of the three mechanisms, the total effective-index change is decomposed into its EO, PE, and TO components under identical operating conditions. As summarized in Figure 8, the EO term dominates under normal drive, as expected from the strong Pockels response of LN. The PE and TO terms are smaller but non-negligible and, depending on the local strain and temperature distribution, can either reinforce or partially offset the EO contribution. Quantitatively, at V_0 = 5 V and ΔT = 0, the Voltage-synchronous photoelastic contribution $\Delta n_{PE,V\text{-}sync}$ = -4.5×10^{-7} is only ~0.6% of the pure Pockels term $\Delta n_{EO} = -1.17 \times 10^{-4}$. Under thermal load (ΔT = 60 K) with operating bias (one electrode driven, the other grounded), the mode-field-weighted V-independent thermal residual $\Delta n_{thermal,mode} = -3.1 \times 10^{-5}$ (or -6.3×10^{-6} in spatial average) is approximately 27% (or 5.4% spatially-averaged) of the modulation depth at V_0= 5 V. Furthermore, comparing the pure Pockels slope at T = 25 °C and T = 85 °Creveals that the EO modulation efficiency itself is thermally stable to within 1.5% (the explicit 25 °C / 85 °C FEM co-simulation reported in Figure 5 yields slopes of -2.342×10^{-5} V^{-1} and -2.343×10^{-5} V^{-1}, respectively, differing by 0.01%, well within this bound), indicating that the dominant temperature-driven term is a V-independent bias offset rather than a degradation of modulation efficiency. Pockels-only analysis therefore captures the modulation signal accurately to within ~10%, but misses the V-independent thermal bias channel that determines bias drift in sensor-grade operation.

Two implications follow from this decomposition. Firstly, a model that retains only the Pockels term systematically mispredicts the magnitude of the phase response. For a FOG application, this results in calibration errors in the scale factor [37]. Secondly, the PE and TO channels are the ones that couple the modulator to its mechanical and thermal environment. Consequently, they are precisely the channels that determine bias drift and environmental sensitivity. Within the domain of evaluating a TFLN modulator for sensing applications, there arises a necessity for the incorporation of the aforementioned elements into the assessment framework.

 doi:10.20944/preprints202605.1502.v1

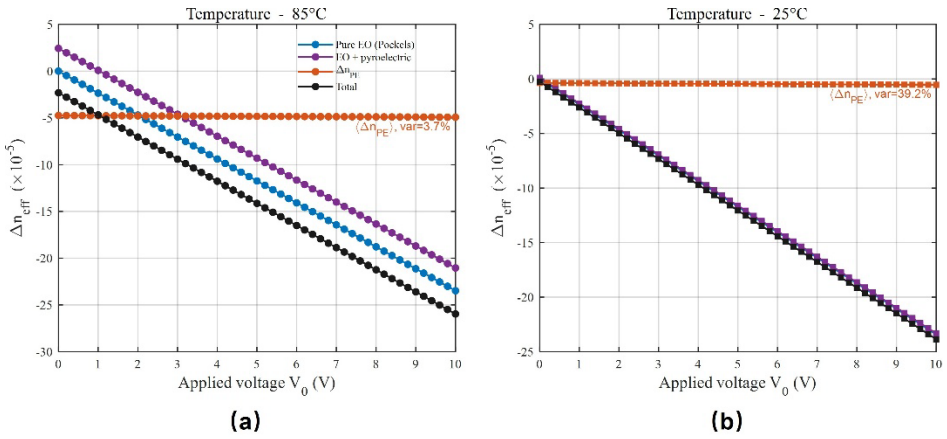

Figure 8. Multiphysics decomposition of the mode-averaged effective-index change at V_0 = 5 V and ΔT = 60K (85 °C): EO (Pockels), V-synchronous PE, and V-independent thermal (pyroelectric + thermo-elastic PE) contributions. Panels: (a) 85 °C; (b) 25 °C.

3.6. Geometry Optimization for Sensor-Oriented Performance

By establishing the multiphysics model, the optimization of the three dominant geometric parameters is now underway: slab thickness h_{slab}, ridge top width w_{top}, and electrode gap g are optimized to balance modulation efficiency and environmental robustness. The three parameters were examined independently as they pertained to the tracking of Γ, $V_\pi L$, and the sensitivity of the phase response to the PE and TO channels.

Slab thickness mainly controls the modal confinement in the ridge [38–40]. Thinner slabs concentrate the field in the ridge region and improve Γ, but excessive thinning increases scattering loss, reduces fabrication tolerance, and aggravates the lateral thermal non-uniformity highlighted in Section 3.4. The optimum is found at h_{slab} = 300 nm, which corresponds to leaving the unetched LN slab at its as-deposited thickness on a 600 nm device-layer wafer (equivalent to a 300 nm ridge etch depth).

Ridge top width sets the modal size and its overlap with the lateral field. Too narrow a ridge improves Γ but increases sidewall-scattering loss and tightens lithography tolerance; too wide a ridge reduces Γ and dilutes the modulation. The optimum lies at an intermediate value. Although the bare $V_\pi L$ exhibits a shallow local minimum at $w_{top} \approx 1.0$ μm at 85 °C, this narrow-ridge regime is excluded from the operating window by single-mode constraints and lithography tolerance, both of which are tighter at sub-1.2 μm ridge widths in TFLN platforms [39].

Figure 9 summarizes the geometric optimization at both operating temperatures. The optical confinement factor Γ_{opt} and the TE purity remain essentially flat at 0.94 ± 0.01 over the entire (w_{top}, h_{slab}) sweep range at both 25 °C and 85 °C, confirming that the targeted quasi-TE_{00} mode is robustly tracked across the design space and that residual variations in $V_\pi L$ reflect genuine modulation-efficiency changes rather than mode-tracking artifacts. Within the swept range, $V_\pi L$ varies in a narrow window (1.665~1.697 V·cm push-pull at 25 °C) and exhibits a shallow plateau spanning $w_{top} \approx$ 1.40~1.45 μm and $h_{slab} \approx$ 200~300 nm, within which the selected operating point (h_{slab} = 300 nm, w_{top} = 1.45 μm) lies. At 85 °Cthe $V_\pi L$ landscape is uniformly elevated by ~17% while preserving the same plateau shape and geometric optimum.

 doi:10.20944/preprints202605.1502.v1

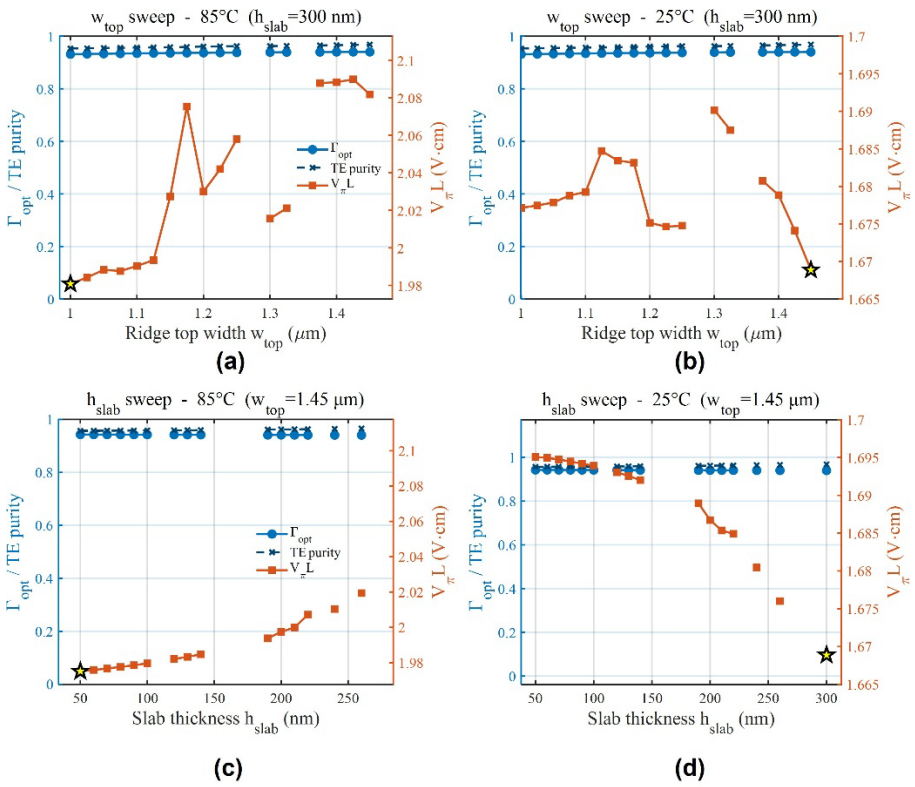

Figure 9. Geometric optimization of the TFLN ridge phase modulator. Ridge-top-width wtop sweep at (a) 85 °C and (b) 25 °C, with slab thickness fixed at h_{slab} = 300 nm. Slab-thickness h_{slab} sweep at (c) 85 °C and (d) 25 °C, with ridge top width fixed at w_{top} = 1.45 μm. Electrode gap g = 5 μm. Left axis: optical confinement factor Γ_{opt} and TE purity; right axis: half-wave voltage-length product $V_\pi L$ (push-pull single-pass). Yellow stars mark the $V_\pi L$ minimum within the swept range; the selected operating point (h_{slab} = 300 nm, w_{top} = 1.45 μm) is determined jointly with the electrode-gap sweep in the subsequent figure.

Optimum at h_{slab} = 300 nm, w_{top} = 1.45 μm, g = 4.4 μm at 25 °C (or 4.2 μm at 85 °C; see Figure 10 for the FoM$_A$ vs gap sweep at both temperatures) yields $V_\pi L$ = 1.65 V·cm (push-pull single-pass) with $\Gamma_{EO} \approx 0.545$, optical confinement factor Γ_{opt} = 0.940, and propagation loss $\alpha \approx 0.26$ dB/cm at the 25 °C optimum. The selected gap of 4.4 μm (25 °C) is dictated by an explicit $V_\pi L$–loss trade-off: reducing the gap further would lower $V_\pi L$ only modestly while raising the propagation loss exponentially through metal-induced absorption - at gap = 2.8 μm, $V_\pi L$ drops to 1.62 V·cm (push-pull) but α already exceeds 5.9 dB/cm; below gap = 2 μm α grows to > 200 dB/cm, rendering any centimeter-scale device non-functional. We therefore introduce a composite figure of merit FoM$_A$ = $V_\pi L$ (V·cm) + $\alpha \cdot L_{ref}$ (dB), with L_{ref} = 1 cm, and minimize it over the gap sweep; the FoM$_A$ minimum occurs at gap = 4.4 μm at 25 °C (FoM$_A$ = 2.23) and shifts marginally to 4.2 μm at 85 °C (FoM$_A$ = 2.56). In this geometry the optical confinement factor Γ_{opt} remains essentially unchanged from its baseline value (0.940 across the entire optimization range), confirming that the modal field stays well-localized in the LN ridge and that the $V_\pi L$ reduction comes purely from the increase in Γ_{EO} as the field approaches the LN core, not from any redistribution of the optical mode itself. At 85 °C the optimal geometry remains essentially unchanged (h_{slab} = 300 nm, w_{top} = 1.45 μm, g = 4.2 μm), while VπL rises modestly to 1.93 V·cm (push-pull single-pass) — a ~17% increase attributable to the intrinsic temperature dependence of the Pockels coefficient γ_{33}, consistent with reported LN material data. This drift is uniform across the (h_{slab}, w_{top}) design space (see Figure 9), preserving the optimal geometry and remaining fully correctable by gain calibration in the FOG read-out electronics

The electrode gap controls the lateral field strength and therefore the EO response most directly. Narrower gaps lower $V_\pi L$ but raise the risk of optical absorption in the metal and increase alignment

 doi:10.20944/preprints202605.1502.v1

sensitivity during fabrication. The chosen value of gap = 4.4 μm (or 4.2 μm at elevated operating temperature) provides the best overall balance.

Compared with the initial design (gap = 5 μm), the optimized geometry reduces $V_\pi L$ by 3% (from 1.70 to 1.65 V·cm push-pull, single-pass); the more meaningful improvement is in the joint $V_\pi L$–α trade-off captured by FoM$_A$, which decreases from 2.95 (gap = 5 μm) to 2.23 (gap = 4.4 μm) at 25 °C. The PE and TO bias perturbations remain essentially unchanged across geometries because they are dominated by the LN material constants and the thermal field, not by the local geometry — a robustness property that simplifies multiphysics-aware design.

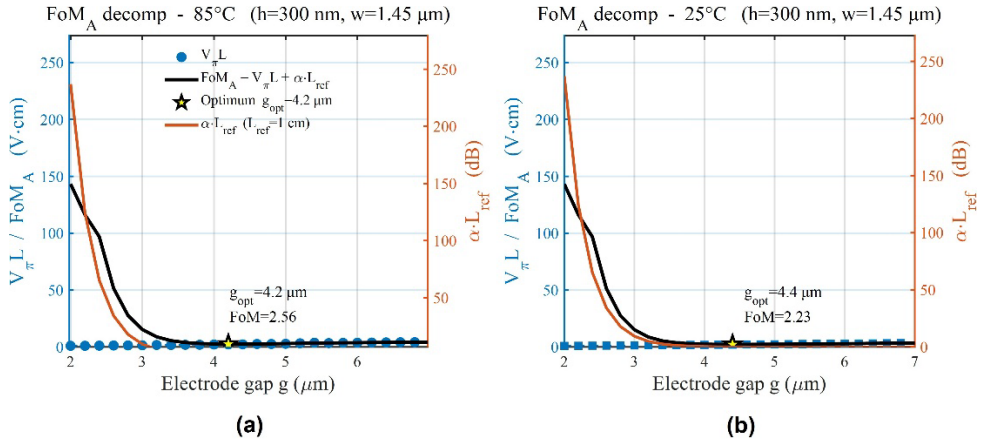

Figure 10. Electrode-gap optimization at the optimal waveguide cross-section (h_{slab} = 300 nm, w_{top} = 1.45 μm). Panels (a) 85 °C and (b) 25 °C: half-wave voltage-length product $V_\pi L$ (push-pull, single-pass; blue dots, left axis), normalized propagation loss $\alpha \cdot L_{ref}$ with L_{ref} = 1 cm (red curve, right axis), and the composite figure of merit FoMA = VπL + α·Lref (black curve, left axis) versus electrode gap g. Yellow stars indicate the minimum FoM$_A$, defining the optimal gaps g= 4.2 μm at 85 °C (FoM$_A$ = 2.56) and 4.4 μm at 25 °C (FoM$_A$ = 2.23).

Table 2. Device performance before and after optimization. All $V_\pi L$ values are reported under the push-pull single-pass convention used throughout this work; the corresponding system-level values in reflective FOG operation are half of the listed numbers.

Parameters	Origin gap =5 μm	Optimization gap =4.4 μm(@25 °C)	Improvement
n_{eff}	1.9034	1.940	+0.4%
Γ_{opt}	0.838	0.940	+12.2%
Γ_{EO}	0.540	0.545	+0.9%
$V\pi \cdot L$@△T=60K	1.70 V·cm	1.65 V·cm	-2.9%
$\triangle n_{PE\ bias}$@△T=60K	-4.5×10^{-7}	-4.5×10^{-7}	PE slope ratio ~ (0.4%)
$\triangle\phi$	0.084π rad/cm	0.083π rad/cm	< 1% (geometry-independent)

3.7. Comparison with Competing Platforms and Implications for FOG Integration

Table 3 compares the present device with representative phase-modulator platforms reported to date. Conventional Ti: $LiNbO_3$ modulators remain the de-facto FOG standard because of their linear Pockels response, but their centimeter-scale footprint and several-volt driving requirement are mismatched with the miniaturization trend. Silicon and InP modulators achieve attractive compactness but either rely on a nonlinear plasma-dispersion effect (Si) or require active temperature stabilization (InP), both of which compromise sensing-grade phase fidelity. Prior TFLN phase modulators, while outstanding for communications, have not been characterized under the full electro-opto-mechano-thermal coupling that governs their use in FOGs. The present device inherits the compactness, linear Pockels response, and low loss of the TFLN platform, and in addition is the

 doi:10.20944/preprints202605.1502.v1

first, to the best of our knowledge, to be co-designed against the PE and TO channels that set the phase-bias stability inside a FOG.

Table 3. Comparison of integrated phase-modulator platforms relevant to fiber-optic gyroscopes.

Platform	V_π (V)	$V_\pi L$ (V·cm)	Footprint	Thermal / mechanical analysis	Sensing suitability
Bulk Ti: $LiNbO_3$ (Applied in conventional FOG [41])	3~5	≈ 10~15	cm-scale	EO only; DC drift known but not co-modeled	Mature, but bulky and power-hungry
Silicon / SOI [42]	5~7	≈ 1~2	mm-scale	EO only (plasma-dispersion, nonlinear)	Compact, but nonlinear response unsuitable for interferometric sensing
InP [43]	1.5~2	≈ 1~2	mm-scale	EO only; TEC mandatory	Compact, but active cooling limits FOG integration
TFLN (prior reports, communication-oriented [44])	1.4~3	≈ 2~3	mm-scale	EO only; PE/TO rarely coupled	High efficiency, but sensing-grade stability not validated
This work (TFLN, sensing-oriented)	**1.65 V (@1cm)**	**1.65**	**mm-scale**	**EO + piezoelectric-PE + thermo-optic + pyroelectric coupled**	**Sensor-grade stability predicted by full multiphysics**

4. Conclusions

We have presented a unified multiphysics model of a thin-film lithium niobate ridge phase modulator designed for fiber-optic gyroscope operation. By self-consistently coupling the electro-optic, piezoelectric–photoelastic, and thermo-optic channels under realistic operating boundary conditions, we have shown that the V-driven response is dominated by the Pockels term while V-independent thermal effects (pyroelectric and thermo-elastic photoelastic, combined ~27% of the modulation depth at $V = 5$ V at $\Delta T = 60$ K) act as bounded bias offsets that are routinely omitted from communication-oriented analyses but must be quantified for sensor-grade design. The geometric EO overlap (Γ_{EO}) is thermally stable to within 0.02% from 25 °C to 85 °C, while the bare VπL increases modestly from 1.65 to 1.93 V·cm due to the intrinsic temperature dependence of γ_{33}. This uniform efficiency change is correctable by gain calibration in the FOG read-out electronics, so the principal environmental concern remains bias drift rather than modulation-efficiency degradation. A systematic optimization of the slab thickness, ridge top width, and electrode gap yields a device with $V_\pi L$ = 1.65 V·cm (push-pull single-pass) with quantified V-synchronous photoelastic and V-

 doi:10.20944/preprints202605.1502.v1

independent thermal residual contributions bounded to ~0.4% and ~27% (mode-field-weighted) of the modulation depth, respectively.

It is important to note that the V-synchronous PE component is thermally invariant, exhibiting a variation of approximately 1% between 25 °C and 85 °C In contrast, the V-independent thermal-elastic PE component demonstrates a substantial increase, reaching approximately thirteenfold with an increase in temperature of 60 K. This phenomenon is only resolvable through coupled multiphysics analysis and is not observed in telecom-oriented $V_{\pi}L$-only characterizations.

Benchmarked against conventional bulk LN, silicon, InP, and prior communication-oriented TFLN modulators, the present device combines a compact footprint, a linear Pockels response, and, for the first time, an explicit multiphysics budget for environmental stability, positioning it as a promising phase-modulator platform for compact, low-power, and thermally robust FOGs. Future work will focus on experimental validation of the predicted multiphysics budget against fabricated devices, and on extending the framework to integrated polarization maintaining interfaces required for full FOG chip-scale integration.

Author Contributions: Conceptualization, L.L. and H.Z.; methodology, J.B. and R.F.; software, H.Z.; validation, Y.C. and Y.W.; formal analysis, W.C.; investigation, W.C.; writing—original draft preparation, L.L. and H.Z.; writing—review and editing, Y.C. and J.B.; funding acquisition, L.L. All authors have read and agreed to the published version of the manuscript.

Funding: This research was funded by the National Key R&D Program of China (2022YFD2000600).

Data Availability Statement: The original contributions presented in this study are included in the article/Supplementary Materials. Further inquiries can be directed to the corresponding author.

Conflicts of Interest: The authors declare no conflicts of interest.

References

1. Lefèvre, H.C. The Fiber-Optic Gyroscope, 2nd ed.; Artech House: Boston, MA, USA, 2014; ISBN 978-1-60807-695-6.
2. Sanders, G.A.; Szafraniec, B.; Liu, R.Y.; Laskoskie, C.; Strandjord, L.; Weed, G. Fiber optic gyros for space, marine, and aviation applications. Proc. SPIE 1996, 2837, 61–71.
3. Yan, L.; Ma, H.; Jin, Z. Low-drift closed-loop fiber optic gyroscope with high scale factor stability. Photonic Sens. 2022, 12, 220304.
4. Zhou, Y.; Hu, X.; Zhang, L.; Liu, Z. Reduction in temperature-dependent FOG bias drift by using MIOC fabricated on pre-annealed LiNbO3. Photonics 2024, 11, 1057.
5. Wooten, E.L.; Kissa, K.M.; Yi-Yan, A.; Murphy, E.J.; Lafaw, D.A.; Hallemeier, P.F.; Maack, D.; Attanasio, D.V.; Fritz, D.J.; McBrien, G.J.; et al. A review of lithium niobate modulators for fiber-optic communications systems. IEEE J. Sel. Top. Quantum Electron. 2000, 6, 69–82.
6. Salvestrini, J.P.; Guilbert, L.; Fontana, M.; Abarkan, M.; Grill, S. Analysis and control of the DC drift in LiNbO3-based Mach-Zehnder modulators. J. Lightwave Technol. 2011, 29, 1522–1534.
7. Rahim, A.; Spuesens, T.; Baets, R.; Bogaerts, W. Open-access silicon photonics platforms in Europe. IEEE J. Sel. Top. Quantum Electron. 2019, 25, 8200818.
8. Ogiso, Y.; Ozaki, J.; Ueda, Y.; Kashio, N.; Kikuchi, N.; Yamada, E.; Tanobe, H.; Kanazawa, S.; Yamazaki, H.; Ohiso, Y.; et al. Over 67 GHz bandwidth and 1.5 V Vπ InP-based optical IQ modulator with InGaAsP-InP bulk structure. J. Lightwave Technol. 2017, 35, 1450–1455.
9. Luo, J.; Jen, A.K.-Y. Highly efficient nonlinear optical polymers and their applications. Nat. Photonics 2022, 16, 605–622.
10. Cheng, R.; Reimer, C.; Kang, Y.; Gehl, M.; Chang, L.; Bowers, J.E.; Englund, D.R. A chip-scale, cryogenic, high-bandwidth optical modulator for practical quantum systems. Nat. Commun. 2023, 14, 7872.
11. Smit, M.; Van der Tol, J.; Hill, M. Moore's law in photonics. Laser Photonics Rev. 2012, 6, 1–13.

 doi:10.20944/preprints202605.1502.v1

12. Smit, M.; Leijtens, X.; Ambrosius, H.; Bente, E.; van der Tol, J.; Smalbrugge, B.; de Vries, T.; Geluk, E.-J.; Bolk, J.; van Veldhoven, R.; et al. An introduction to InP-based generic integration technology. Semicond. Sci. Technol. 2014, 29, 083001.
13. Wang, C.; Zhang, M.; Chen, X.; Bertrand, M.; Shams-Ansari, A.; Chandrasekhar, S.; Winzer, P.; Lončar, M. Integrated lithium niobate electro-optic modulators operating at CMOS-compatible voltages. Nature 2018, 562, 101–104.
14. Xu, M.; He, M.; Zhang, H.; Jian, J.; Pan, Y.; Liu, X.; Chen, Z.; Meng, X.; Chen, H.; Li, Z.; et al. High-performance coherent optical modulators based on thin-film lithium niobate platform. Nat. Commun. 2020, 11, 3911.
15. Boes, A.; Chang, L.; Langrock, C.; Yu, M.; Zhang, M.; Lin, Q.; Lončar, M.; Fejer, M.; Bowers, J.; Mitchell, A. Lithium niobate photonics: Unlocking the electromagnetic spectrum. Science 2023, 379, eabj4396.
16. Zhu, D.; Shao, L.; Yu, M.; Cheng, R.; Desiatov, B.; Xin, C.J.; Hu, Y.; Holzgrafe, J.; Ghosh, S.; Shams-Ansari, A.; et al. Integrated photonics on thin-film lithium niobate. Adv. Opt. Photonics 2021, 13, 242–352.
17. Weis, R.S.; Gaylord, T.K. Lithium niobate: Summary of physical properties and crystal structure. Appl. Phys. A 1985, 37, 191–203.
18. Pionteck, T.; Kühnel, K.; Rüsing, M.; Eng, L.M. Photoelastic properties of stoichiometric lithium niobate from first-principles calculations. Phys. Status Solidi A 2024, 221, 2300456.
19. Atalar, A.; Kino, G.S.; Quate, C.F. Longitudinal piezoelectric resonant photoelastic modulator for efficient intensity modulation at megahertz frequencies. Nat. Commun. 2022, 13, 1526.
20. Yin, Q.; Wang, J.; Ma, J.; Li, J. Analysis of pyroelectric effect and thermal properties of lithium niobate under varying temperatures. Crystals 2021, 11, 1434.
21. Shi, B.; Kollipara, T.; Duan, Z.; Yao, J. Alleviation of DC drift in a thin-film lithium niobate modulator utilizing Ar+ ion milling. Opt. Lett. 2025, 50, 1703–1706.
22. Ahmed, A.N.R.; Shi, S.; Mercante, A.J.; Prather, D.W. High-performance thin-film lithium niobate modulator with a combined passive bias and thermo-optic bias. Opt. Express 2022, 30, 39710–39718.
23. Fedulova, E.; Nazabal, V.; Adamietz, F.; Rodriguez, V.; Möller, K.; Villeval, P.; Lupinski, D.; Strickler, P.; Elsa, N. Lithium niobate pyroelectric coefficient: Temperature dependence study. Crystals 2022, 12, 321.
24. Randles, A.B.; Grinberg, D.; Shumarayev, A.; Johansson, A.; Koskinen, J.T. Multiphysics simulation of RF-MEMS devices using COMSOL. J. Micromech. Microeng. 2019, 29, 014003.
25. Gao, Z.; Ding, Z.; Wen, F.; Lv, H.; Xu, T. Navigation-grade interferometric air-core antiresonant fibre optic gyroscope with enhanced thermal stability. Nat. Commun. 2025, 16, 1748.
26. Lu, Y.; Yang, C.; Chen, J.; Zhang, W.; Wang, Y. Integrated optoelectronic transceiver toward navigation grade fiber optic gyroscope using silicon photonics. Opt. Lett. 2025, 50, 7139–7142.
27. Chen, G.; Li, N.; Ng, J.D.; Lin, H.-L.; Zhou, Y.; Fu, Y.H.; Lee, L.Y.T.; Yu, Y.; Liu, A.-Q.; Danner, A.J. Advances in lithium niobate photonics: Development status and perspectives. Adv. Photonics 2022, 4, 034003.
28. Zhang, M.; Wang, C.; Kharel, P.; Zhu, D.; Lončar, M. Integrated lithium niobate electro-optic modulators: when performance meets scalability. Optica 2021, 8, 652–667.
29. Wang, T.; Chen, P.; Shi, J.; Qi, X. High-performance Mach-Zehnder modulator based on thin-film lithium niobate with low voltage-length product. ACS Omega 2023, 8, 12395–12401.
30. Palik, E.D. (Ed.) Handbook of Optical Constants of Solids; Academic Press: Orlando, FL, USA, 1985; ISBN 978-0-12-544420-0.
31. Green, M.A. Self-consistent optical parameters of intrinsic silicon at 300 K including temperature coefficients. Sol. Energy Mater. Sol. Cells 2008, 92, 1305–1310.
32. Johnson, P.B.; Christy, R.W. Optical constants of the noble metals. Phys. Rev. B 1972, 6, 4370–4379.
33. Alferness, R.C. Waveguide electrooptic modulators. IEEE Trans. Microw. Theory Tech. 1982, 30, 1121–1137.
34. Boes, A.; Corcoran, B.; Chang, L.; Bowers, J.; Mitchell, A. Status and potential of lithium niobate on insulator (LNOI) for photonic integrated circuits. Laser Photonics Rev. 2018, 12, 1700256.
35. He, M.; Xu, M.; Ren, Y.; Jian, J.; Ruan, Z.; Xu, Y.; Gao, S.; Sun, S.; Wen, X.; Zhou, L.; et al. High-performance hybrid silicon and lithium niobate Mach-Zehnder modulators for 100 Gbit s−1 and beyond. Nat. Photonics 2019, 13, 359–364.

 doi:10.20944/preprints202605.1502.v1

36. Mercante, A.J.; Shi, S.; Yao, P.; Xie, L.; Weikle, R.M.; Prather, D.W. 110 GHz CMOS compatible thin film LiNbO3 modulator on silicon. Opt. Express 2016, 24, 15590–15595.
37. Jiao, D.; Zhou, H. Interferometric fiber optic gyroscope with thin-film lithium niobate modulator chip. J. Lightwave Technol. 2024, 42, 8912–8920.
38. Liu, X.; Wang, M.; Rao, D.; Ke, W. Design and analysis of compact high-performance lithium niobate electro-optic modulator based on a racetrack resonator. Photonics 2025, 12, 85.
39. Li, M.; Ling, J.; He, Y.; Javid, U.A.; Xue, S.; Lin, Q. Lithium niobate photonic-crystal electro-optic modulator. Nat. Commun. 2020, 11, 4123.
40. Kang, G. Shallow etched low-loss thin-film lithium niobate waveguides with bound states in the continuum. AIP Adv. 2023, 13, 035332.
41. Javid, U.A.; Ling, J.; Staffa, J.; Li, M.; He, Y.; Lin, Q. Ultrabroadband entangled photons on a nanophotonic chip. Phys. Rev. Lett. 2021, 127, 183601.
42. Jiao, D.; Zhou, H. Bias instability 0.09 deg/h interferometric fiber optic gyroscope with thin-film lithium niobate modulator chip. IEEE Photonics Technol. Lett. 2024, 36, 1021–1024.
43. Liu, J.; Yin, M.; Yu, B.; Wang, D.; Zhang, T.; Fu, X. Multi-channel thin-film lithium niobate photonic integrated circuit for fiber optic gyroscope applications. Photonics 2025, 12, 213.
44. Gustavsen, K.; Brodal, J.P.; Breunig, I.; Lemke, N.D. Navigation-grade hollow-core photonic bandgap fiber optic gyroscope at 1550 nm. Nat. Commun. 2025, 16, 2083.